RSC Advances

PAPER

View Article Online
View Journal | View Issue

Cite this: *RSC Adv.*, 2017, **7**, 27354

3D nanostructured $WO_3/BiVO_4$ heterojunction derived from *Papilio paris* for efficient water splitting†

Chao Yin, Shenmin Zhu* and Di Zhang*

Received 26th March 2017
Accepted 5th May 2017

DOI: 10.1039/c7ra03491a

rsc.li/rsc-advances

We report on a novel butterfly wing-like $WO_3/BiVO_4$ heterojunction for photocatalytic water splitting, in which $BiVO_4$ is the primary visible light-absorber and WO_3 acts as an electron conductor. The heterojunction, which is prepared by a one-step sol–gel method, achieves high light absorption and charge separation efficiencies, even without a sacrificial agent, and produces a photocatalytic O_2 evolution of 20 μmol h^{-1} mg^{-1} under visible light irradiation (λ > 420 nm) and an incident photon-to-current conversion efficiency of ~10% at 380–450 nm, both at a potential of 1.23 V *versus* RHE. Compared to planar $WO_3/BiVO_4$ heterojunction, the 3D nanostructured $WO_3/BiVO_4$ heterojunction shows significantly improved photocatalytic performance due to the quasi-honeycomb structure inherited from the *Papilio paris* and the efficient separation of the photogenerated charge at the $WO_3/BiVO_4$ interface. Synthesis details are discussed, with heterojunction morphologies and structures characterized by field emission scanning electron microscopy and X-ray diffraction.

Introduction

Photocatalytic water splitting into H_2 and O_2 using semiconductors is a very attractive and desirable way to meet the global energy challenge and solve environmental issues.[1,2] Although several semiconductor materials show photocatalytic activity, most of them have limited utility due to the high charge carrier recombination[3] and wide band gaps, which make them only active under UV light irradiation, and UV light represents merely 4–5% of the solar spectrum energy lies.[4] A range of attempts have been made to improve light absorption and charge separation efficiencies, including impurity doping,[5–7] loading co-catalysts,[8,9] and the introduction of nanoscale porosity.[10,11] Moreover, photocatalytic performance has also been improved by the formation of heterojunctions, which couple a large band gap semiconductor with a small band gap semiconductor. Heterojunctions have a more negative conduction band (CB) level, and the CB electrons can be injected from the small band gap semiconductor into the large band gap semiconductor, promising that the heterojunction can be more efficient than a single semiconductor system.[12]

Monoclinic $BiVO_4$ ($mBiVO_4$) has become the top performer among all metal oxide photocatalysts under visible light owing to its relatively small band-gap energy (2.4 eV).[13] $BiVO_4$ based heterostructures with other desirable semiconductors including ZnO,[14] WO_3,[12,15–19] nanowires of Fe_2O_3 (ref. 20) and others[21–24] have been shown to promote the separation of electron–hole pairs and anti-photocorrosion. Among the latest state-of-the-art $BiVO_4$-based heterojunctions, the highest efficiency was achieved by a W doped $WO_3/BiVO_4$ core/shell nanowire photoanode, synthesized on an FTO without an added catalyst, which produced a photocurrent of 3.1 mA cm^{-2} under simulated sunlight and an incident photon-to-current conversion efficiency of ~60% at 300–450 nm, both at a potential of 1.23 V *versus* RHE.[12] However, the cumbersome process and difficulty in controlling the nanomorphology of the photoanode create obstacles in its practical use.

As a matter of fact, nature offers an astonishing variety of materials with exquisite 3D hierarchical structures, which cannot be easily synthesized using available nanotechnology to date. 3D hierarchical structures from nature often display an efficient light-harvesting capacity, particularly in the region of visible light, and the abundant biogenic elements endowed from biological systems can be preserved and incorporated into the final biotemplated materials to reduce the bandgap of photocatalysts,[25] leading to a new way to obtain efficient photocatalysts. Recently, we reported that a C-doped $BiVO_4$ photocatalyst with fine 3D hierarchical structures templated from *Papilio paris* butterfly wings fabricated by a novel one-step sol–gel and templating method enables simultaneous control of crystal phase, nanomorphology, and element carbon doping in a single process.[26] The improved photocatalytic performance was attributed to the synergetic effect of the unique morphology and doping control. We have also reported that the sequence of

State Key Laboratory of Metal Matrix Composites, Shanghai Jiao Tong University, 800 Dongchuan Road, Shanghai, 200240, P. R. China. E-mail: smzhu@sjtu.edu.cn; zhangdi@sjtu.edu.cn; Fax: +86-21-34202749; Tel: +86-21-34203927

† Electronic supplementary information (ESI) available. See DOI: 10.1039/c7ra03491a

ceramic WO_3 butterfly wings was also inherited from *Papilio paris*.[27] We verified that the quasi-honeycomb structure adapted from *Papilio paris* can help WO_3 harvest visible light more efficiently and boost charge transport. Nevertheless, the efficiency of these photocatalysts is not sufficient due to the still limited charge separation efficiencies. Hence heterojunction nanoarchitectures coupled with the unique structures are expected to result in the highest photocatalytic activity.

In this study, we fabricate a novel 3D nanostructured WO_3/$BiVO_4$ heterojunction derived from *Papilio paris* for photocatalytic water splitting, in which $BiVO_4$ is the primary visible light-absorber and WO_3 acts as an electron conductor. The heterojunction, which is prepared by a one-step sol–gel method, achieves the highest light absorption and charge separation efficiencies among $BiVO_4$-based powder composites, even without a sacrificial agent. In the following, we will describe the synthesis and characterization of the present WO_3/$BiVO_4$ heterojunction in detail and explain the origin of the improved photocatalytic performance.

Experimental

Materials

Butterfly wing biotemplates were purchased from Shanghai Natural Wild-Insect Kingdom Co., Ltd. Analytical grade reagents such as phosphotungstic acid 44-hydrate ($H_3PO_{40}W_{12}$), bismuth nitrate ($Bi(NO_3)_3 \cdot 5H_2O$), ammonium metavanadate (NH_4VO_3), ethanol, acetic acid, nitric acid, and tetramethylammonium hydroxide (TMAH) were purchased from Sinopharm Reagent Chemical Co., Ltd.

Synthesis

In a typical synthesis, first, *Papilio paris* butterfly wings, as biological templates, were air dried before use. The biological samples were pretreated by a mixture solution of acetic acid and ethanol for 6 h at room temperature and then washed with deionized water and air-dried for 24 h. The pretreated samples were carefully dipped into 20 wt% of phosphotungstic acid 44-hydrate ($H_3PO_{40}W_{12}$) in ethanol solution and kept at 36 °C for 6 h, denoted as WO_3BWs.[27] Then, WO_3/$BiVO_4$ heterojunction was achieved by a one-step sol–gel method and a two-step sol–gel method. In the one-step sol–gel process, WO_3BWs were washed with ethanol and dried overnight under vacuum at 60 °C and dipped into the $BiVO_4$ sol–gel solution[26] and kept at 36 °C for 12 h. Finally, the samples were calcined in air at 500 °C with a constant heating rate of 1 °C min^{-1} to format the crystal and remove the organic templates (WO_3/$BiVO_4$BWs). The synthesis process is illustrated in Scheme 1. For comparison, WO_3/$BiVO_4$BWs (two-step) were prepared by WO_3BWs, which were first calcined in N_2 atmosphere at 800 °C to crystallize the WO_3 and dipped into the $BiVO_4$ sol–gel solution at last.

Photocatalytic activity test

The photocatalytic activities of the samples were evaluated by the amount of oxygen split from water (Labsolar-H_2, Perfect Light, China) under visible light. Portions of the solid samples

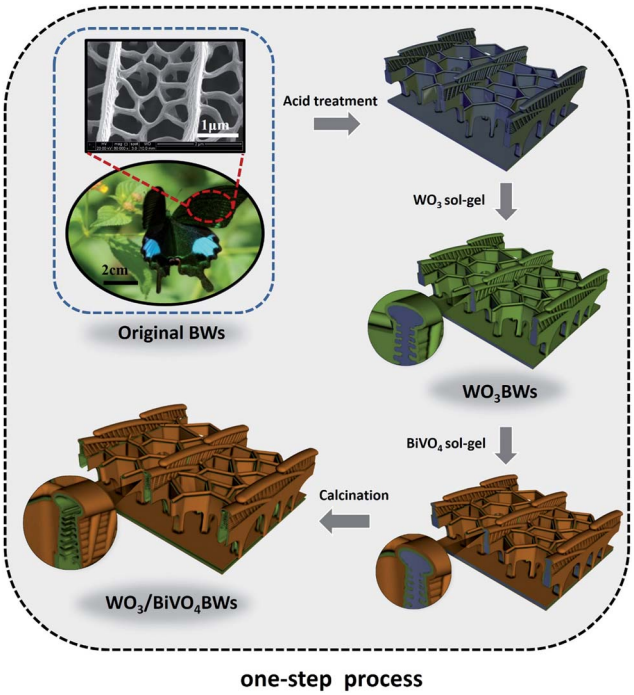

Scheme 1 The synthesis process of replication of butterfly wing in WO_3/$BiVO_4$BWs.

(10 mg) were introduced into a spectroscopic quartz probe cell, and the measurements were taken at room temperature under visible light irradiation from a 300 W Xe lamp (PLS-SXE300/300UV, Perfect Light, China) equipped with a cutoff filter L42. The visible light intensity is about 10 mA. The evolved gases were analyzed by gas chromatography with a thermal conductivity detector (GC7890II, Tianmei, Shanghai; N_2 carrier gas).

The electrodes were prepared according to the method from Kudo. Photoelectrochemical properties were evaluated with a three-electrode cell consisting of the prepared electrodes, a Pt electrode, and a saturated Ag/AgCl electrode as the working, counter, and reference electrodes, respectively. The working electrode was irradiated from the FTO side with visible-light through a cutoff filter (L42). The incident photon-to-photocurrent efficiency (IPCE) was calculated as follows:

$$[\text{IPCE}/\%] = 1240 \times [\text{photocurrent density}/\mu\text{A cm}^{-2}]/([\text{wavelength}/\text{nm}] \times [\text{photo flux}/\text{Wm}^{-2}])$$

Characterizations

The synthesized samples were examined by X-ray diffraction (XRD) on a D-max/2550 (Rigaku) X-ray diffractometer system operating at 1600 W power (40 kV, 40 mA) with Cu Kα radiation ($\lambda = 0.15406$ nm), at a scan rate of 4° min^{-1} and a step size of 0.050° in 2θ. The morphologies and microstructures of the samples were characterized using a FEI QUANTA TEG 250 scanning electron microscope (SEM) and a JEOL2011 transmission electron microscope (TEM). TEM specimens were

prepared by dispersing the synthesized samples in pure ethanol, and the powder was picked up by copper grids. UV-Visible (UV-Vis) diffuse reflectance spectra of all the samples were recorded using a PerkinElmer UV-Vis-NIR spectrophotometer (750S) in the spectral range of 200–800 nm, and Raman scattering measurements were obtained in back scattering geometry on a Via^{+} Reflex from 150–1000 cm^{-1}.

Results and discussion

$BiVO_4$ has a narrow band gap (2.4 eV), and its conduction band is more negative than that of WO_3. Therefore coupling with photocorrosion resistant WO_3, WO_3/$BiVO_4$ heterojunctions[15–19] could be suitable for efficient photocatalytic water splitting under visible irradiation; see Fig. 1e. The quasi-honeycomb structure of *Papilio paris* butterfly wings is shown in Fig. S1,† which can absorb visible light to an utmost degree with over 95% absorption rate.[28] The morphologies of WO_3BWs, WO_3/$BiVO_4$BWs (two-step) and WO_3/$BiVO_4$BWs are shown in Fig. 1a–c. The quasi-honeycomb and three-layer structures of the scales can clearly be seen in the three samples. Compared with the original butterfly wing, the replicas show a 20% shrinkage for both WO_3/$BiVO_4$BWs (two-step) and WO_3/$BiVO_4$BWs after calcination (Fig. 1b and c). The scales, neatly arranged on the surface of the structure of the *Papilio paris* butterfly wings, were completely retained by WO_3 (Fig. 1a). The parallel ridges of the scales and nanoscale ribs were retained in the WO_3/$BiVO_4$BWs, indicating an extremely fine duplication of the original scale structures using the one-step sol–gel method (Fig. 1c), and the high-resolution TEM (HRTEM) images provide the 150 nm average pore diameter (Fig. 1d). However, the further finer and elaborate architectures in the ribs of the WO_3/$BiVO_4$BWs (two-step) disappear (Fig. 1b) because of the significant grain growth of WO_3 particles when the calcination temperature reaches 800 °C, suggesting a poor photocatalytic performance.

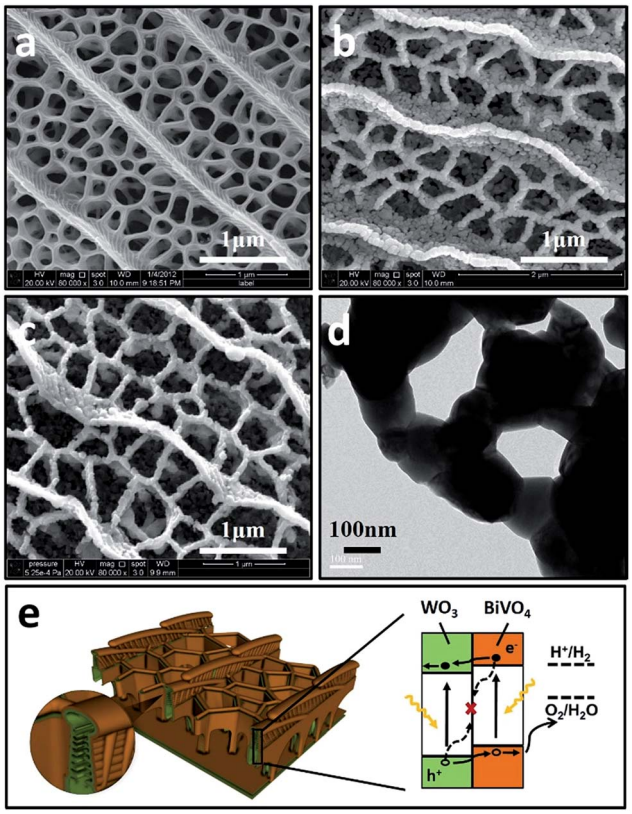

Fig. 1 The 3D nanostructured WO_3/$BiVO_4$BWs. (a–c) Scanning electron microscope (SEM) of WO_3BWs, WO_3/$BiVO_4$BWs (two-step) and WO_3/$BiVO_4$BWs. (d) Transmission electron microscope (TEM) images of the WO_3/$BiVO_4$BWs (150 nm average pore diameter). The $BiVO_4$ consists of a single layer of densely packed nanoparticles. (e) Structural schematic and energy band diagram of the butterfly wing WO_3/$BiVO_4$BWs and type-II staggered heterojunction, in which charges generated in both the $BiVO_4$ outside and WO_3 inside can contribute to water oxidation. The band edges and water oxidation and reduction potentials are plotted on the reversible hydrogen electrode (RHE) scale.

Fig. 2a shows X-ray diffraction patterns of WO_3BWs, $BiVO_4$-BWs, and WO_3/$BiVO_4$BWs. In the WO_3BWs, the peaks of 23.3, 23.8, and 24.6° are observed corresponding to (002), (020), and (200) planes for the monoclinic phase of WO_3 (JCPDS 43-1035), which is known to show the highest photocatalytic effect compared to other crystal phases.[29,30] Compared with monoclinic WO_3, several new peaks appeared on the XRD spectra, and they could be indexed as other W_xO_y phases, such as $WO_{2.9}$ and $W_{18}O_{49}$. This means that the bio-template resulted in multiple

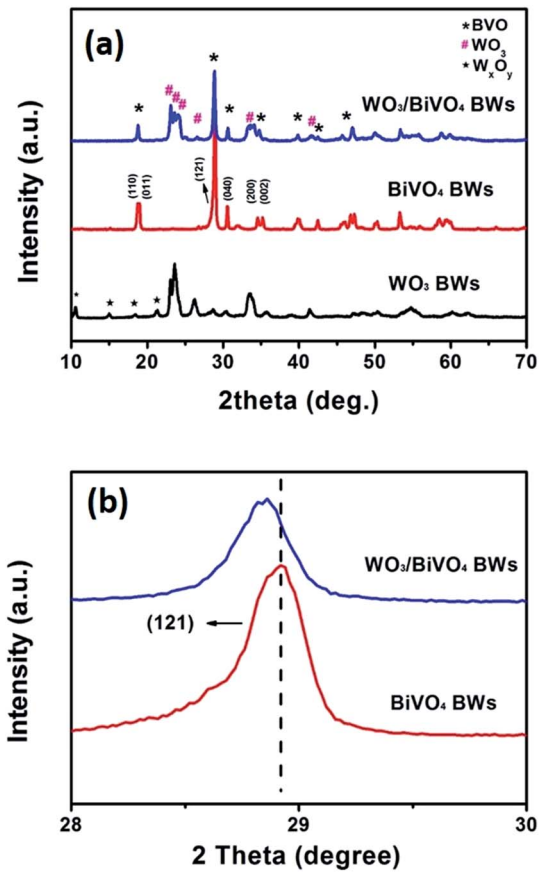

Fig. 2 XRD patterns of (a) WO_3BWs, $BiVO_4$BWs, and WO_3/$BiVO_4$BWs. (b) Magnified peaks of (120) planes in the range of 2θ from 28° to 30°.

tungsten oxide phases in the replicas. For bare $BiVO_4$BWs, the main peaks can be indexed as (110), (011), (121), (040), (200) and (002) planes, which can represent the monoclinic $BiVO_4$ (JCPDS 14-0688) without any impurity phase, illustrating that the bio-template has been removed completely by calcination at 500 °C. In the case of WO_3/$BiVO_4$BWs, monoclinic WO_3 and $BiVO_4$ are the only phases detected in XRD measurements (Fig. 2a), demonstrating that a novel 3D nanostructured WO_3/$BiVO_4$ heterojunction derived from *Papilio paris* with pure and high crystallinity can be achieved by the one-step sol–gel method mentioned before. As a result, the average grain size of the samples, calculated *via* the Scherrer formula, are 15.3, 27.2 and 30.5 nm, corresponding to WO_3BWs, $BiVO_4$BWs, and WO_3/$BiVO_4$BWs, respectively, while WO_3/$BiVO_4$BWs (two-step) shows 48.5 nm.

Fig. 2b exhibits a magnified view of (121) peaks, which show 0.318° shifts to lower angles in the WO_3/$BiVO_4$BWs, compared with the $BiVO_4$BWs. Pratap M. Rao *et al.* in 2014 have reported that W^{6+} dopes into $BiVO_4$ by substituting for V^{5+} and acts as an electron donor in the WO_3/$BiVO_4$ core/shell nanowire photoanode.[12] This shifting may be ascribed to lattice expansion due to the slight portion of W atoms incorporating from WO_3. These XRD results indicate that little W atoms have been well inserted into V sites of the host $BiVO_4$ lattice, induces lattice expansion without forming any segregated impurity phase.[12] It has been known that impurity doping may form new bonds to promote the electron–hole separation efficiency.[6] Therefore, the WO_3/$BiVO_4$BWs are expected to show enhanced photocatalytic performance.

Moreover, Fig. 3 presents the Raman spectra of the WO_3BWs, $BiVO_4$BWs, and WO_3/$BiVO_4$BWs in the 150–1000 cm^{-1} region. The bands at 827, 723, 367, 324, 210 and 128 cm^{-1} in the $BiVO_4$BWs correspond to the typical vibrations of monoclinic $BiVO_4$. The band at 827 is assigned to the typical symmetric V–O stretching mode,[31] and the one with a weak shoulder at about 712 cm^{-1} assigned to the antisymmetric V–O stretching mode, whereas those at 367 and 324 cm^{-1} are attributed to the typical symmetric and antisymmetric bending modes of the vanadate anion.[32,33] Raman vibrations centered at 135, 214, 708 and 785 cm^{-1}, characteristic of pure WO_3, are also detected in the WO_3BWs. The bands at 708 and 785 cm^{-1} are identified as the O–W–O bending and stretching mode, respectively.[32]

AS seen from Fig. 3, in the case of WO_3/$BiVO_4$BWs, it is clear that a shift of the Raman band to the lower wavenumber, from 827 to 810 cm^{-1} assigned to symmetric V–O bond stretching mode, reveals that the average lone-range symmetry of the VO_4 tetrahedral becomes less regular. The blue-shift is due to the W-doping effect where W has been inserted into the V sites of the $BiVO_4$ lattice to form the W–O bond, which has the bond length shorter than that of the V–O bond. Furthermore, the band at 785 cm^{-1} attributed to O–W–O bonds is broad and shifted to 810 cm^{-1} in WO_3/$BiVO_4$BWs, probably due to the formation of the WO_3/$BiVO_4$ heterojunction structures, which generate a new W–O–V bond,[33] consistent with XRD results. It has been reported that formation of new bonds can promote electron–hole separation efficiency of photocatalysts. It would be expected that WO_3/$BiVO_4$BWs should perform the best in the photocatalytic O_2 production experiments.

To investigate the optical absorption properties of the samples, UV/Vis spectroscopy was conducted, and the results are shown in Fig. 4. Light absorption of the bare WO_3BWs starts at around 475 nm in correspondence with its band gap energy. For the bare $BiVO_4$BWs, the onset of light absorption is around 520 nm, again corresponding to its band gap energy. In the WO_3/$BiVO_4$BWs, the main absorption edge has a red-shift of more than 20 nm compared with pure $BiVO_4$BWs. It indicates that the band-gap energy of the samples is affected by the quasi-honeycomb structure of *Papilio paris* butterfly wing, and the quasi-honeycomb structure can enhance visible light absorption, which has been reported by us before.[26] Moreover, compared with $BiVO_4$BWs and WO_3BWs, WO_3/$BiVO_4$BWs exhibits an increased photoabsorption at wavelengths between 200 nm and 480 nm, which is probably due to the formation of the heterojunction structure. The optical band-gap energies of the three samples are estimated from the absorption spectra using the following relationship:

$$\alpha h\nu = A(h\nu - E_g)^n$$

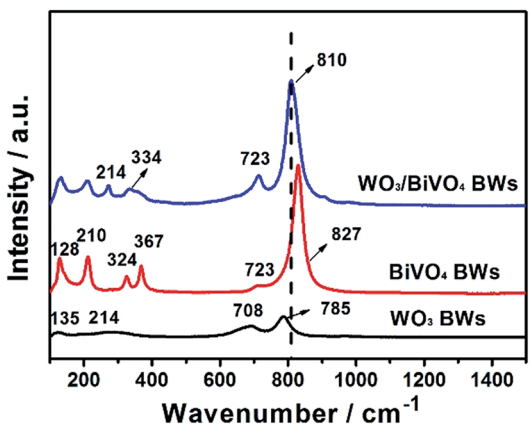

Fig. 3 Raman spectra of WO_3BWs, $BiVO_4$BWs, and WO_3/$BiVO_4$BWs.

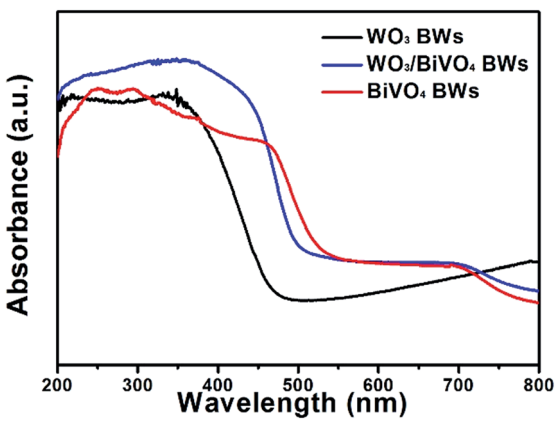

Fig. 4 UV-Vis absorbance spectra of WO_3BWs, $BiVO_4$BWs, and WO_3/$BiVO_4$BWs.

where E_g is the band-gap energy of allowed transitions (eV), h is Planck's constant (6.626×10^{-34} J s), α and ν are the absorption coefficient and light frequency, respectively, and A is a constant. The band gap energy for $BiVO_4$BWs is measured to be about 2.4 eV, which is smaller than that of WO_3/$BiVO_4$BWs (2.46 eV) and WO_3BWs (2.69 eV). Thus, the absorption range of the WO_3BWs is enhanced by coupling of $BiVO_4$ having a smaller band gap energy. Thus, the band-gap energy of the samples is affected by the quasi-honeycomb structure of *Papilio paris* butterfly wings and the heterojunction coupled by WO_3 and $BiVO_4$. The small difference in band gap has a significant influence on the photocatalytic performance, which will be discussed later with the results of oxygen production from water splitting.

We further measure photocurrents of WO_3BWs, $BiVO_4$BWs, and WO_3/$BiVO_4$BWs by depositing each material on ITO electrodes. A fast and strong photocurrent response is observed for each switch-on/off event in both WO_3/$BiVO_4$BWs and $BiVO_4$-BWs-deposited electrodes under visible light (Fig. 5a). Under visible light irradiation ($\lambda > 420$ nm), the photocurrent of WO_3/$BiVO_4$BWs electrode (2.5 μA) is approximately 5 times higher than that of the $BiVO_4$BWs electrode (0.5 μA), which indicates that the separation efficiency of photo-induced electrons and holes is improved significantly through the electronic interaction between $BiVO_4$ and WO_3, as expected from the results in Fig. 5a. In contrast, no photocurrent is recorded for WO_3BWs under visible light irradiation, which implies no photocatalytic O_2 evolution from water splitting under visible light gap.

The incident photon-to-photocurrent efficiency (IPCE) spectra of WO_3BWs, $BiVO_4$BWs, and WO_3/$BiVO_4$BWs are shown in Fig. 5b, in which the electrodes are measured at 1.23 V (*vs.* Ag/AgCl) in 0.5 M Na_2SO_4 using monochromatic light controlled with band pass filters. The IPCE is defined by the following equation:

$$[\text{IPCE}/\%] = 1240 \times [\text{photocurrent density}/\mu\text{A cm}^{-2}]/([\text{wavelength}/\text{nm}] \times [\text{photo flux}/\text{Wm}^{-2}])$$

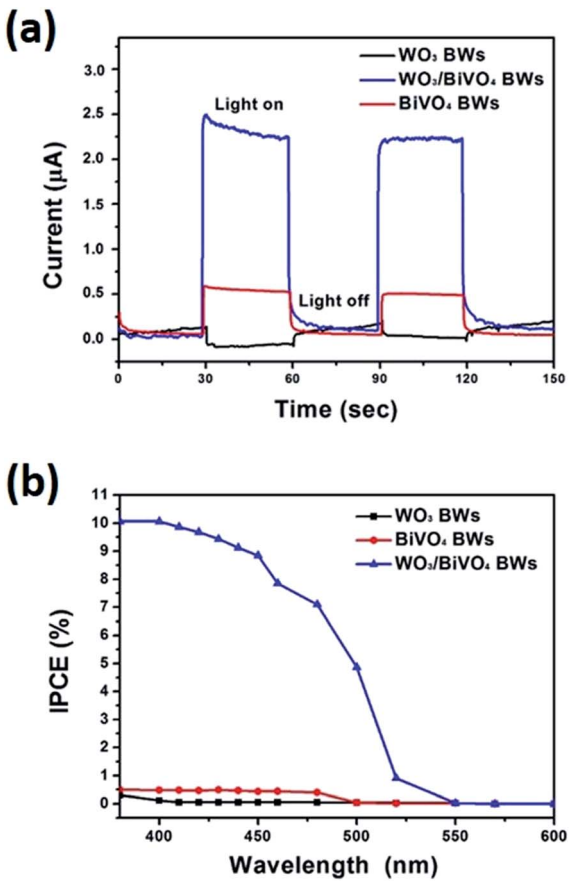

Fig. 5 (a) Photocurrent responses of WO_3BWs, $BiVO_4$BWs, and WO_3/$BiVO_4$BWs under visible light irradiation ($\lambda > 420$ nm). (b) Incident photon to current conversion efficiency (IPCE) of the WO_3BWs, $BiVO_4$BWs, and WO_3/$BiVO_4$BWs. The IPCE was measured at 1.23 V (*vs.* Ag/AgCl) under 0.5 M Na_2SO_4 solution. The three-electrode cell consists of a prepared electrode, a Pt electrode, and a saturated Ag/AgCl electrode as the working, counter, and reference electrodes, respectively. The working electrode was irradiated from the FTO side with visible-light through a cutoff filter (L42).

The WO_3BWs shows rising IPCE from 480 nm and the $BiVO_4$BWs from 540 nm, in agreement with their band gap energies. The WO_3/$BiVO_4$BWs also shows the onset of IPCE at 540 nm similar to $BiVO_4$BWs. Moreover, the WO_3/$BiVO_4$BWs electrode performs at an excellent anodic photocurrent with 10.8% of an IPCE at 400 nm at 1.23 V *vs.* Ag/AgCl, whereas the trivial IPCE of WO_3BWs at 0.3% (at 380 nm) and $BiVO_4$BWs at 0.7% (at 400 nm) is observed. Despite the range of light absorption of $BiVO_4$BWs being larger than WO_3/$BiVO_4$BWs, the photoactivity was much less because of poor charge transfer characteristics as evidenced by the photocurrents study discussed above. Because WO_3 cannot absorb light with wavelength between 500 and 540 nm, the IPCE in this range for WO_3/$BiVO_4$BWs originates from the absorption by the $BiVO_4$ layers. However, unlike bare $BiVO_4$, the WO_3/$BiVO_4$ heterojunction can utilize light at 500–540 nm for water oxidation because the good charge transfer characteristic at the interface induces rapid transfer of photoelectrons formed in $BiVO_4$ to WO_3. One order of magnitude enhancement in photoconversion efficiency indicates that WO_3/$BiVO_4$BWs may result in the best photocatalytic activity.

On the basis of the above results, the photocatalytic activities of the samples were tested for O_2 evolution from water splitting under visible light range. Fig. 6 shows the amount of evolved O_2 by solar light from boiled water. The amount of evolved O_2 from aqueous solution after 1 h from the WO_3/$BiVO_4$BWs is *ca.* 200 μmol, which is 5 times as much as that of the $BiVO_4$BWs (*ca.* 42 μmol), the highest photocatalytic O_2 evolution among all the tested samples. The total evolved O_2 after 5 h from the WO_3/$BiVO_4$BWs is *ca.* 950 μmol, which is more than 7.6 times that of the $BiVO_4$BWs (*ca.* 125 μmol). On the contrary, WO_3/$BiVO_4$BWs (two-step) shows *ca.* 35 μmol (Fig. S2, ESI†) and WO_3BWs produces no oxygen under visible light irradiation. The results suggest that the WO_3/$BiVO_4$BWs performs the best photocatalytic activities, compared with other hierarchical porous photocatalysts from bio-templates that we have reported

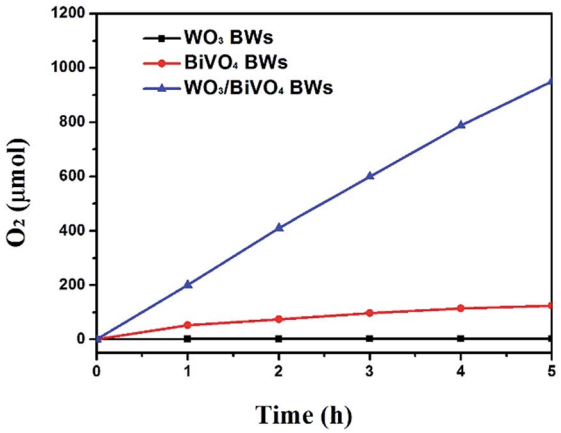

Fig. 6 Photocatalytic O_2 evolution of WO_3BWs, $BiVO_4$BWs, and WO_3/$BiVO_4$BWs under visible light irradiation (λ > 420 nm). The amount is kept the same for all the samples.

before.[26,27] This result shows that the WO_3/$BiVO_4$BWs are stable and indeed oxidize water into O_2.

From all the results presented above, a possible mechanism for photocatalytic O_2 evolution from water splitting by the WO_3/$BiVO_4$BWs has been proposed and illustrated in Fig. 7. We attribute the significantly enhanced photocatalytic performance of WO_3/$BiVO_4$BWs under visible light to more absorption of visible light as well as more efficient transfer of photogenerated electrons. The unique quasi-honeycomb structure allows more visible light waves to penetrate deep inside the photocatalyst, thus improving the light absorption capability and the formation of heterojunctions which enhances the separation of photogenerated electron–hole pairs and thus reduces charge recombination rate as evidenced by the photocurrent responses analysis.

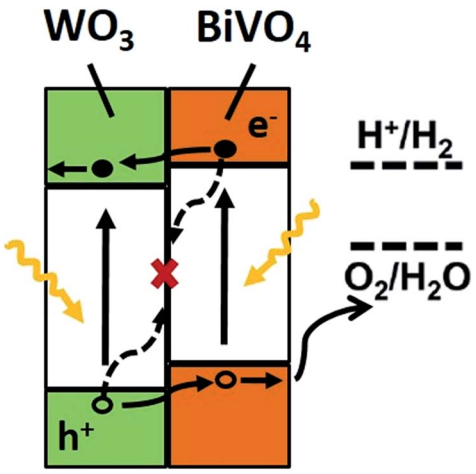

Fig. 7 Depiction of the energy diagram of the WO_3/$BiVO_4$ heterojunction (at pH 7) and electron transport process. Suggested mechanism for the photocatalytic O_2 evolution by WO_3/$BiVO_4$BWs under visible-light. The conduction band of WO_3 and $BiVO_4$ are −0.52, and 0.05 eV, respectively. Electrons from $BiVO_4$ flow to the conduction band of WO_3. Valence electrons of $BiVO_4$ are excited to the conduction band state by absorbing visible light, which can convert oxygen molecules in the solution to singlet oxygen.

According to the literature, for a WO_3 film in Na_2SO_4, a flat-band potential of V_{fb} = 0.15 V (*vs.* SCE) was reported by Patil,[34] while the V_{fb} of $BiVO_4$ was reported as −0.62 V (*vs.* SCE) by Sayama[35] and Li[36]. It is generally known that the bottoms of the conduction bands in several n-type semiconductors are more negative by 0.1 V than the flat band potential.[37] In the photocatalytic oxygen evolution process (Fig. 7), illumination photons create electron–hole pairs in the WO_3/$BiVO_4$BWs at the solid/solution interface. These electron–hole pairs separate and reach the photocatalyst surface by diffusion. Owing to the positive conduction band position (>0 eV *vs.* NHE at pH = 7), only the reaction of holes with water to produce O_2 can occur spontaneously (eqn (2)).

$$h\nu \xrightarrow{BiVO_4} e^- + h^+ \quad (1)$$

$$2H_2O + 4h^+ \rightarrow 4H^+ + O_2 \quad (2)$$

With the bottom of the $BiVO_4$ conduction band more positive than that of WO_3, it is favorable for the electrons to travel from the $BiVO_4$ conduction band to WO_3. Hence, electrons generated in the $BiVO_4$ will first travel radially inward to the WO_3 in the WO_3/$BiVO_4$BWs, and then travel to the current collector through WO_3, in turn suppressing electron–hole recombination. Although $BiVO_4$ absorbs a larger fraction of solar light than WO_3 due to its narrower band gap as shown in Fig. 4, electrons and holes formed in $BiVO_4$ are not fully utilized for water decomposition reaction because its poor transfer characteristics lead to recombination. However, the holes can migrate to the semiconductor/electrolyte interface either directly or after transfer from WO_3 to $BiVO_4$. The reduced recombination naturally induces photoactivity enhancement.

Conclusions

In summary, a novel 3D nanostructured WO_3/$BiVO_4$ heterojunction derived from *Papilio paris* for photocatalytic water splitting is fabricated by a one-step sol–gel method. The quasi-honeycomb structure of the original butterfly wings is kept perfectly in the heterojunction. The photocurrents of WO_3/$BiVO_4$BWs (2.5 μA) is approximately 5 times higher than that of a $BiVO_4$BWs (0.5 μA), and an incident photon-to-current conversion efficiency of ~10% at 380–450 nm (1.23 V *versus* RHE), indicating a higher product of light absorption and charge separation efficiencies. The WO_3/$BiVO_4$BWs, in which $BiVO_4$ is the primary visible light-absorber and WO_3 acts as an electron conductor, achieved an excellent photocatalytic O_2 evolution of 20 μmol h^{-1} mg^{-1} under visible light irradiation, which is 5 times higher than $BiVO_4$BWs, even without a sacrificial agent. The enhanced photocatalytic performance is attributed to not only the unique quasi-honeycomb structure with an efficient visible light-harvesting capacity, but also to improved separation efficiency of photo-induced electrons and holes through the electronic interaction in the WO_3/$BiVO_4$ heterojunction. These promising results open new possibilities in the

design of highly photoactive heterojunction photocatalysts inherited from bio-templates for water-splitting systems.

Acknowledgements

The authors gratefully acknowledge financial support for this research from the Morgan Crucible Company, the National Science Foundation of China (No. 51072117, 51171110), the National Basic Research Program of China (973 Program, 2012CB619600), the Shanghai Science and Technology Committee (0JC1407600). We also thank the Shanghai Jiao Tong University (SJTU) Instrument Analysis Center.

Notes and references

1 A. Kudo and Y. Miseki, *Chem. Soc. Rev.*, 2009, **38**, 253–278.
2 M. G. Walter, E. L. Warren, J. R. McKone, S. W. Boettcher, Q. Mi, E. A. Santori and N. S. Lewis, *Chem. Rev.*, 2010, **110**, 6446.
3 H. P. Maruska and A. K. Ghosh, *Sol. Energy Mater.*, 1979, **1**, 411–429.
4 P. V. Kamat, *Chem. Rev.*, 1993, **93**, 267–300.
5 W. J. Jo, J. W. Jang, K. J. Kong, H. J. Kang, J. Y. Kim, H. Jun, K. P. S. Parmar and J. S. Lee, *Angew. Chem., Int. Ed.*, 2012, **51**, 1–6.
6 W. J. Luo, Z. S. Yang, Z. Li, J. Zhang, J. Liu, Z. Zhao, Z. Wang, S. Yan, T. Yu and Z. Zou, *Energy Environ. Sci.*, 2011, **4**, 4046–4051.
7 S. K. Pilli, T. E. Furtak, L. D. Brown, T. G. Deutsch, J. A. Turner and A. M. Herring, *Energy Environ. Sci.*, 2011, **4**, 5028–5034.
8 F. Lin, D. G. Wang, Z. X. Jiang, Y. Ma, J. Li, R. Li and C. Li, *Energy Environ. Sci.*, 2012, **5**, 6400–6406.
9 J. A. Seabold and K. S. Choi, *J. Am. Chem. Soc.*, 2012, **134**, 2186–2192.
10 R. G. Li, F. X. Zhang, D. G. Wang, J. X. Yang, M. R. Li, J. Zhu, X. Zhou, H. X. Han and C. Li, *Nat. Commun.*, 2013, **4**, 1–7.
11 L. Chen, Q. Zhang, R. Huang, S. F. Yin, S. L. Luo and C. T. Au, *Dalton Trans.*, 2012, **41**, 9513–9518.
12 P. M. Rao, L. Cai, C. Liu, I. S. Cho, C. H. Lee, J. M. Weisse, P. Yang and X. Zheng, *Nano Lett.*, 2014, **14**, 1099–1105.
13 A. Kudo, K. Omori and H. Kato, *J. Am. Chem. Soc.*, 1999, **121**, 11459–11467.
14 T. W. Kim and K. S. Choi, *Science*, 2014, **343**, 990–994.
15 W. J. Luo, Z. S. Yang, Z. Li, J. Zhang, J. Liu, Z. Zhao, Z. Wang, S. Yan, T. Yu and Z. Zou, *Energy Environ. Sci.*, 2011, **4**, 4046–4051.
16 S. J. A. Moniz, J. Zhu and J. W. Tang, *Adv. Energy Mater.*, 2014, **4**, 1301590.
17 R. Saito, Y. Miseki and K. Sayama, *Chem. Commun.*, 2012, **48**, 3833–3835.
18 S. J. Hong, S. Lee, J. S. Jang and J. S. Lee, *Energy Environ. Sci.*, 2011, **4**, 1781–1787.
19 K. Zhang, X. J. Shi, J. K. Kim and J. H. Park, *Phys. Chem. Chem. Phys.*, 2012, **14**, 11119–11124.
20 J. Su, L. Guo, N. Bao and C. A. Grimes, *Nano Lett.*, 2011, **11**, 1928–1933.
21 Y. Hou, F. Zuo, A. Dagg and P. Feng, *Nano Lett.*, 2012, **12**, 6464–6473.
22 A. Iwase, Y. H. Ng, Y. Ishiguro, A. Kudo and R. Amal, *J. Am. Chem. Soc.*, 2011, **133**, 11054–11057.
23 F. F. Abdi, L. Han, A. H. M. Smets, M. Zeman, B. Dam and R. vande Krol, *Nat. Commun.*, 2013, **4**, 2195.
24 X. Lin, Y. S. Wang, J. Zheng, C. Liu, Y. Yang and G. B. Che, *Dalton Trans.*, 2015, **44**, 19185–19193.
25 C. J. Li, S. P. Wang, T. Wang, Y. J. Wei, P. Zhang and J. L. Gong, *Small*, 2014, **10**, 2783–2790.
26 C. Yin, S. M. Zhu, Z. X. Chen, W. Zhang, J. J. Gua and D. Zhang, *J. Mater. Chem. A*, 2013, **1**, 8367–8378.
27 C. Yin, S. M. Zhu, F. Yao, J. J. Gu, W. Zhang, Z. X. Chen and D. Zhang, *J. Nanopart. Res.*, 2013, **15**, 1812–1823.
28 P. Vukusic, J. R. Sambles and C. R. Lawrence, *Proc. R. Soc. B*, 2004, **271**, 237–239.
29 U. M. García-Pérez, S. Sepúlveda-Guzmán and A. Martínez-de la Cruz, *Solid State Sci.*, 2012, **14**, 293–298.
30 J. Kenneth, M. Donald and K. S. Choi, *Energy Environ. Sci.*, 2012, **5**, 8553–8557.
31 H. Liu, R. Nakamur and N. Yoshihiro, *J. Electrochem. Soc.*, 2005, **152**, 856–861.
32 G. S. Li, D. Q. Zhang and J. C. Yu, *Chem. Mater.*, 2008, **20**, 3983–3992.
33 D. Wang, H. Jiang, X. Zong, Q. Xu, Y. Ma, G. Li and C. Li, *Chem.–Eur. J.*, 2011, **17**, 1275–1282.
34 P. S. Patil and P. R. Patil, *Bull. Mater. Sci.*, 1996, **19**, 651–656.
35 K. Sayama, A. Nomura, T. Arai, T. Sugita, R. Abe, M. Yanagida, T. Oi, Y. Iwasaki, Y. Abe and H. J. Sugihara, *J. Phys. Chem. B*, 2006, **110**, 11352–11360.
36 M. Li, Z. L. Hao and L. Guo, *Int. J. Hydrogen Energy*, 2010, **35**, 7127–7133.
37 Y. Matsumoto, K. Omae, I. Watanabe and E. J. Sato, *J. Electrochem. Soc.*, 1986, **133**, 711–716.

